The Astrophysical Journal Letters, 920:L38 (7pp), 2021 October 20 https://doi.org/10.3847/2041-8213/ac2c7c

Molecules and Outflows in NML Cygni: New Insights from a 1 mm Spectral Line Survey

A. P. Singh[1], J. L. Edwards[1,3], R. M. Humphreys[2], and L. M. Ziurys[1]
[1] Department of Chemistry, Department of Astronomy and Steward Observatory, Arizona Radio Observatory, University of Arizona, Tucson, AZ 85721, USA
lziurys@email.arizona.edu
[2] Minnesota Institute for Astrophysics, University of Minnesota, Minneapolis, MN 55455, USA
Received 2021 June 1; revised 2021 September 28; accepted 2021 September 30; published 2021 October 18

Abstract

A sensitive (1σ rms $\leqslant 3$ mK) 1 mm spectral survey (214.5–285.5 GHz) of the oxygen-rich circumstellar envelope of the red hypergiant NML Cygni (NML Cyg) has been conducted using the Sub-millimeter Telescope (SMT) of the Arizona Radio Observatory (ARO). Over 100 spectral lines were detected, arising from 17 different molecules, including the carbon-bearing species CO, HCN, HCO^+, CN, and HNC; sulfur- and silicon-containing compounds H_2S, SO, SO_2, SiO, and SiS; and more exotic NaCl and AlO. The 1 mm spectrum of NML Cyg closely resembles that of VY Canis Majoris (VY CMa) suggesting that the chemistries of hypergiant stars are similar. The line profiles in NML Cyg consist of multiple velocity features, particularly evident in SO_2 and SO. In addition to a spherical wind at the star's systemic velocity, the spectra suggest an asymmetric, blueshifted component near $V_{LSR} = -21 \pm 3$ km s^{-1} and a collimated, redshifted component near 15 ± 3 km s^{-1}, positioned ∼34° and ∼12°, respectively, from the line of sight. The red- and blueshifted flows appear to be randomly oriented, and likely trace sporadic mass loss events. Their LSR velocities align closely with those of 22 GHz water masers, suggesting an NE–SE orientation. The winds may also be associated with the asymmetric nebula in F555W HST images but extending to 5″ (∼$600R_*$). NML Cyg appears to be another example of rare, massive stars with collimated, episodic ejections, analogous to Betelgeuse and VY CMa, lending support for an important new mass loss mechanism—surface activity.

Unified Astronomy Thesaurus concepts: Circumstellar envelopes (237); Hypergiant stars (774); Millimeter astronomy (1061); Astrochemistry (75); Molecular spectroscopy (2095); Stellar evolution (1599); Stellar mass loss (1613); Stellar winds (1636)

1. Introduction

The majority of stars with masses between ∼9 and 40 $M_\odot$ are thought to pass through the red supergiant (RSG) phase and then undergo a terminal supernova explosion (Smartt 2009). However, more recently there has been evidence that stars with masses greater than ∼18 $M_\odot$ may evolve back to warmer temperatures or quietly collapse into black holes without an explosive stage, becoming "failed" supernovae (e.g., Smartt 2015; Gordon et al. 2016; Davies & Beasor 2020). Hypergiant stars, such as VY Canis Majoris (VY CMa), and IRC+10420, can be viewed as extreme versions of RGSs, characterized by extensive, asymmetric circumstellar shells, with episodic, high mass loss events occurring over the course of several hundred years (e.g., Humphreys et al. 2021; Tiffany et al. 2010). Such mass loss is not understood.

Infrared and submillimeter imaging of dust has revealed the presence of a variety of irregular structures in hypergiant ejecta, including clumps, knots, arcs, and filaments (e.g., Schuster et al. 2009; Shenoy et al. 2016; Kaminski et al. 2013; Kaminski 2019; Humphreys et al. 2007, 2019, 2021; O'Gorman et al. 2015). Spectroscopic measurements have provided velocity information for the gas associated with the dusty structures, indicating spatial orientation and ejection timescales (e.g., Humphreys et al. 2021). In turn, millimeter molecular emission has revealed the presence of asymmetric outflows in VY CMa, establishing their chemical/physical characteristics (Ziurys et al. 2007; Adande et al. 2013; Tenenbaum et al. 2010a, 2010b; De Beck et al. 2015; Decin et al. 2016).

VY CMa is exceptional among hypergiants with its rich molecular envelope and active chemistry (Tenenbaum et al. 2010a, 2010b). With the goal of further probing hypergiant properties, we have conducted a 1 mm spectral line survey of NML Cygni (NML Cyg). NML Cyg is a luminous hypergiant star, with $M \sim 40\,M_\odot$ and a mass loss rate of about $10^{-4}\,M_\odot$ yr^{-1} (Nagayama et al. 2008; Schuster et al. 2009). Located near the Cyg OB2 stellar association at a distance of 1.6 kpc (Zhang et al. 2012a), NML Cyg possesses a dusty envelope like VY CMa (Schuster et al. 2009). Optical images show the shell to have an unusual half-moon shape, oriented NE–SE on 0.″5 spatial scales (Schuster et al. 2006). The inner envelope has been a source of OH, H_2O, and SiO maser emission (Richards et al. 1996; Boboltz & Claussen 2004; Nagayama et al. 2008). The more extended circumstellar envelope contains other molecules, including CO, CO_2, HCN, SO, NH_3, and HCO^+ (Justtanont et al. 1996; Ziurys et al. 2009; Pulliam et al. 2011; Teyssier et al. 2012). More recently, PO and PN have been identified in NML Cyg (Ziurys et al. 2018).

Our spectral survey, carried out at the ARO SMT, shows that the envelope of NML Cyg is very similar to VY CMa. The complete data set for the survey will be presented in a following paper (A. P. Singh et al. 2021, in preparation). Here we describe the highlights of the survey and its implications for the understanding of these unusual stars.

2. Observations

The measurements were conducted between 2008 March and 2014 March using the ARO SMT 10 m antenna located at Mt. Graham, AZ. The dual-polarization receiver employed sideband-separating (SBS) ALMA Band 6 SIS mixers. Image rejection was typically $\geqslant 16$ dB, inherent in the mixer architecture. The

[3] Current Address: Department of Natural Sciences, Gulf Coast State College, Panama City, FL 32401.

temperature scale at the SMT is measured as T_A^*, determined by the chopper wheel method. The radiation temperature T_R is then $T_R = T_A^*/\eta_b$, where η_b is the main beam efficiency; $\eta_b = 0.72$–0.74 across the 1 mm band (214.5–285.5 GHz). The backend used was a 2048 channel filter bank with 1 MHz resolution, operated in parallel mode (2×1024 channels) to accommodate both polarizations.

Data from the survey was collected in 1 GHz frequency intervals over the range of 214.5–285.5 GHz; the total survey required over 800 hr of integration time. The intermediate frequency (IF) was varied between 4.5 and 7.5 GHz, as well as the signal sideband (USB or LSB), to assess image contamination; local oscillator shifts of 20 MHz were also performed. Observations were carried out in beam switching mode with a subreflector throw of ±2′. The position for NML Cyg is $\alpha = 20^h46^m25\overset{s}{.}5$, $\delta = 40°06'59\overset{''}{.}4$ (J2000.0), using $V_{LSR} = -5\ \mathrm{km\ s^{-1}}$ (or $V_{\mathrm{helio}} = -22\ \mathrm{km\ s^{-1}}$). Pointing and focus were done by observation of planets. Linear baselines were removed from all spectra.

3. Results and Analysis

Figure 1 shows the complete 1 mm survey of NML Cyg (second panel), with the scale set at 0.11 K (T_A^*) to show the weaker features. The off-scale lines are CO ($J = 2 \rightarrow 1$), HCN ($J = 3 \rightarrow 2$), and SiO ($J = 5 \rightarrow 4$, $6 \rightarrow 5$). The top panel is the 1 mm ARO SMT survey of VY CMa (Tenenbaum et al. 2010a, 2010b), scale set at 0.21 K, T_A^*. The composite spectra of NML Cyg and VY CMa have a similar set of observed transitions, but with some variation in intensity (see Tenenbaum et al. 2010a). The NML Cyg spectrum has weaker line intensities, likely a result of its greater distance (1.6 kpc versus, 1.2 kpc: Zhang et al. 2012a, 2012b).

The third panel shows a 1 GHz section of the survey centered at 282 GHz, illustrating the varying line profiles in NML Cyg. While the PN transition appears Gaussian in shape, the two stronger SO_2 lines ($J_{\mathrm{Ka,Kc}} = 15_{1,15} \rightarrow 14_{0,14}$(left), $6_{2,4} \rightarrow 5_{1,5}$,(right)) do not. These transitions lie at different energies (93.9 and 29.2 K). Nevertheless, both line profiles exhibit a blueshifted spike-like component near $-20\ \mathrm{km\ s^{-1}}$ and a broader redshifted feature at $\sim 15\ \mathrm{km\ s^{-1}}$, as well as more symmetric emission at the LSR velocity of the star. The blue- and redshifted features are suggestive of asymmetric outflows, as found for VY CMa (Tenenbaum et al. 2010a). A weak, blueshifted feature is also observed in the $J_K = 1_0 \rightarrow 0_0$ transition of NH_3 near $-18\ \mathrm{km\ s^{-1}}$ (Teyssier et al. 2012). The bottom panel shows spectra of NaCl, NS, and AlO.

Table 1 lists the molecules identified in the survey and the number of transitions observed, including isotopic variants; seventeen distinct chemical species were detected, with ^{13}C, ^{29}Si, and ^{30}Si isotopologues measured in CO, HCN, SiO, and SiS. The set of molecules observed in the NML Cyg survey is virtually identical to that for VY CMa, with the exception of AlOH, thus far found only in the latter source (Tenenbaum & Ziurys 2010). Some of the molecules found in the survey have previously been observed toward NML Cyg, as mentioned, as well as NH_3, OH and CO_2 (e.g., Justtanont et al. 1996; Ziurys et al. 2009; Teyssier et al. 2012). New identifications include NaCl, AlO, and NS. PN and PO were reported previously by Ziurys et al. (2018).

Modeling of molecular abundances, relative to H_2, and envelope radial distributions was carried out with the non-LTE radiative transfer code ESCAPADE (Adande et al. 2013). The code, based on the Sobolev approximation, employs the escape probability formalism. Collisional and infrared dust excitation are considered. The code can model collimated (asymmetric) outflows, which are approximated as a cone with a specified direction relative to the line of sight.

For the modeling, the following gas density profile was used (Kemper et al. 2003; Adande et al. 2013):

$$n_{H_2}(r) = \frac{\dot{M}}{4\pi r^2 \left(1 - \frac{R_*}{r}\right) V_{\mathrm{exp.}}}. \quad (1)$$

Here $\dot{M}$ is the average mass loss rate, assumed to be $\sim 10^{-4}\ M_\odot\ \mathrm{yr^{-1}}$ (Schuster et al. 2009), R_* is the stellar radius (2.4×10^{14} cm; Nagayama et al. 2008), and V_{exp} is the average expansion velocity, estimated from the individual line profiles. The gas kinetic temperature profile was based on Zubko et al. (2004) from H_2O measurements (see Ziurys et al. 2009):

$$T_{\mathrm{kin}}(\mathrm{r}) = T_0 \left(\frac{R_0}{r}\right)^{0.5}. \quad (2)$$

Here 270 K is the gas kinetic temperature at $r = 10^{16}$ cm. The calculation for all molecules except AlO and NaCl was started at $r \sim 5 \times 10^{15}$ cm ("r_{inner}"), the assumed maximum radius of the dust formation zone ($\sim 20 R_*$), where the envelope reaches its terminal velocity (Monnier et al. 1997). (For NaCl and AlO, 10 R_* was used.) Based on the relationship $R_{\mathrm{dust}}/R_* \sim (T_*/T_{\mathrm{dust}})^2$ from van Loon et al. (2005), the dust temperature at $r_{\mathrm{inner}} = 5 \times 10^{15}$ cm is estimated to be $T_{\mathrm{dust}} \sim 580$ K, assuming $T_* \sim$ 2500 K (Zhang et al. 2012a). The dust infrared emission was modeled as a blackbody at this temperature. Dust optical constants were not used because the wide range of physical parameters needed for accurate modeling are not known for NML Cyg (see Ysard et al. 2018).

The molecular line profiles in NML Cyg were modeled assuming a spherical (Gaussian) distribution, using the expression (Adande et al. 2013):

$$f(r) = f_0 \exp\left(-\left(\frac{r - r_{\mathrm{inner}}}{r_{\mathrm{outer}}}\right)^2\right). \quad (3)$$

Here f_0 is the maximum abundance, relative to H_2, at r_{inner}, and r_{outer} is the radius at which the abundance drops by a factor of $1/e$. The nonisotropic outflows (SO, SO_2, CS, CO, and HCO^+) were modeled as Gaussian distributions with a maximum abundance f_0 at a distance from the star r_{peak}:

$$f(r) = f_0 \exp\left(-\left(\frac{r - r_{\mathrm{peak}}}{r_{\mathrm{outer}} - r_{\mathrm{peak}}}\right)^2\right). \quad (4)$$

Again, r_{outer} is where the abundance drops by a factor of $1/e$. Fitting parameters include r_{outer},r_{peak}, f_o, expansion velocity, angle with respect to the line of sight (inclination angle), and cone angle. The H_2 density is also modeled (see Adande et al. 2013).

Energy level data were obtained from databases CDMS (Müller et al. 2005), and JPL (Pickett et al. 1998), A coefficients from EXOMOL (Tennyson & Yurchenko 2012) and CDMS, and collisional rates with H_2 from BASECOL (Dubernet et al. 2010). Almost all molecules had an average expansion velocity of $V_{\mathrm{exp}} \sim 16 \pm 3\ \mathrm{km\ s^{-1}}$, except for NaCl and AlO, where it was significantly smaller ($V_{\mathrm{exp}} \sim 9$–$10\ \mathrm{km\ s^{-1}}$: for AlO, corresponding to individual hyperfine components). As has been found in VY CMa (e.g., Ziurys et al. 2007), NaCl, and AlO appear to condense out before the terminal envelope velocity is achieved. Model results are given in Table 1; those for AlO are rough estimates.

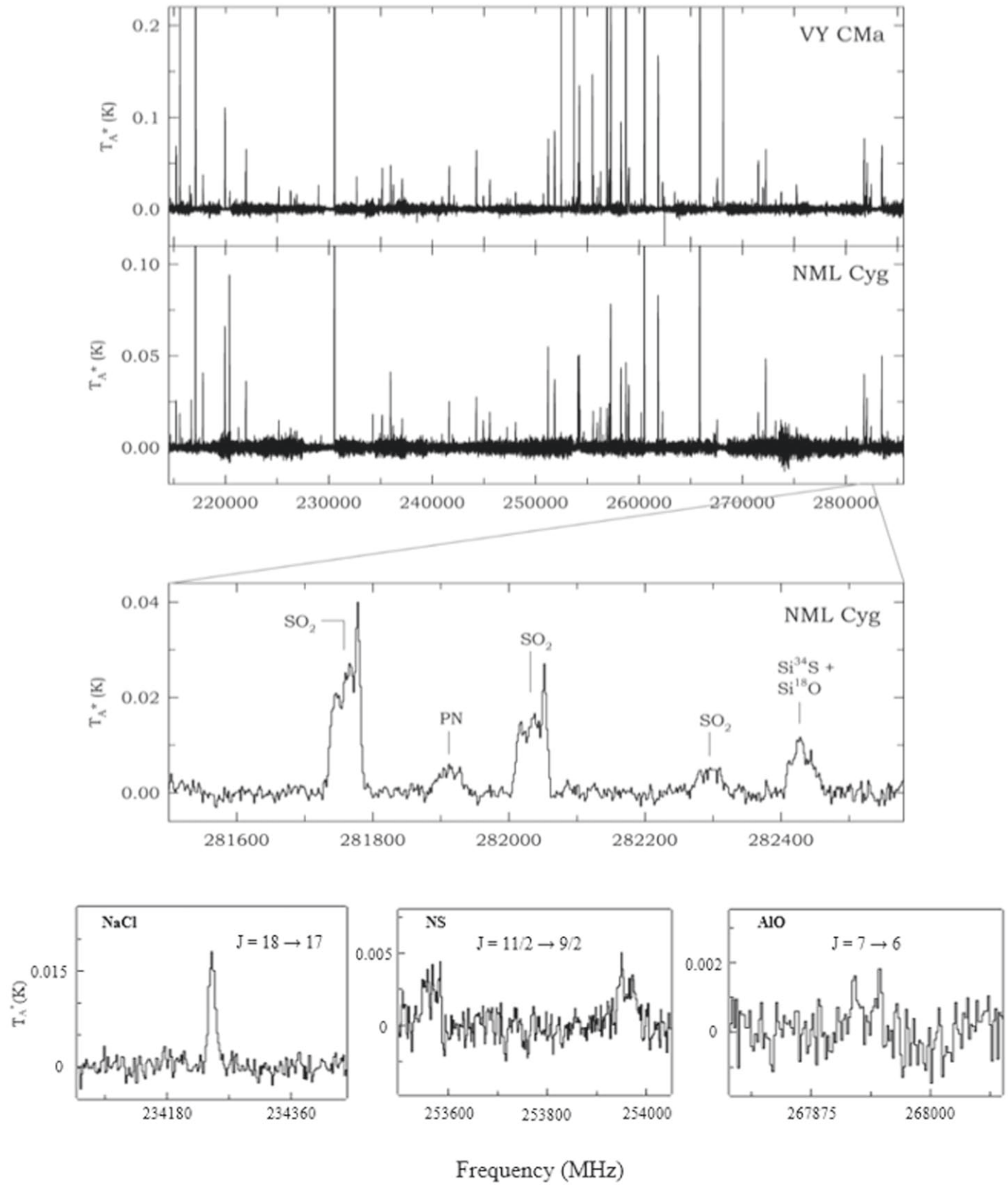

Figure 1. Composite spectrum of the ARO SMT 1 mm survey of NML Cyg (second panel), and an identical survey spectrum of VY CMa (top panel: Tenenbaum et al. 2010a, 2010b). A 1 GHz section of the NML Cyg survey at 282 GHz is also shown (third panel), displaying the asymmetric line profiles in SO_2 and SO. Spectra of NaCl, NS, and AlO (bottom panel) are also displayed (Resolution: 2 MHz).

Table 1
Molecules Identified in the Envelope of NML Cyg

Number	Molecule	Transitions	$f(X/H_2)$[f]	r_{outer}[f]	
				(R_*)	($''$)
1	CO	3[a]	3.5×10^{-4}	330	2.7
2	SiO	2	8.0×10^{-7}	180	1.5
3	SiS	4	3.5×10^{-7}	160	1.3
4	SO	5	3.5×10^{-7}	230	1.9
5	CS	1	3.0×10^{-8}	170	1.4
6	CN	2[a]	2.0×10^{-7}	250	2.0
7	NS	2	2.0×10^{-9}	170	1.3
8	H_2S	2	4.5×10^{-6}	300	2.4
9	NaCl	12[a]	4.5×10^{-9}	45	0.4
10	PN[b]	2	3.0×10^{-9}	170	1.4
11	PO[b]	4	1.0×10^{-8}	280	2.3
12	AlO	1	$\sim 6 \times 10^{-9}$	~25	~0.2
13	HCN	2[a]	3.6×10^{-7}	320	2.6
14	HNC	1	2.0×10^{-8}	140	1.1
15	SO_2	32	6.5×10^{-7}	190	1.5
16	HCO^+[c]	4	…	…	…
17	H_2O	1	…	…	…
18	NH_3[d]	…	…	…	…
19	OH[d]	…	…	…	…
20	CO_2[e]	…	…	…	…

Notes.
[a] Includes isotopic species.
[b] Ziurys et al. (2018).
[c] Pulliam et al. (2011).
[d] Teyssier et al. (2012).
[e] Justtanont et al. (1996).
[f] Spherical flow; $r_{inner} \sim 20R_*$; $10R_*$ for AlO, NaCl.

Uncertainties in the modeling results are ~5%–20%, depending on the number of observed transitions and their signal-to-noise ratios. As a test, the inner radius for NaCl was changed by a factor of 2, but the results remained within our quoted uncertainties.

For SO, SO_2, CS, and CO, a three-component fit was carried out, with central (spherical, as described), blueshifted and redshifted features (Adande et al. 2013). The fits for the red and blue outflows are summarized in Table 2. For SO, the lowest 70 energy levels of ground state and the first 43 levels of the first excited vibrational state ($v = 1$) were included, while for SO_2, 198 ground state levels and 168 $v_2 = 1$ were used. Use of additional energy levels produced less than 5% abundance difference. For CO and CS, the lowest 23 and 21 levels for the $v = 0$ state were included in the calculation, respectively, and the lowest 20 for $v = 1$. The HCO^+ data (Pulliam et al. 2011) was also reanalyzed with a two-component fit (red and blue flows), with 31 and 36 levels ($v = 0$ and $v = 1$).

Sample spectra and three components fits for SO and SO_2 are shown in Figure 2. The fits are shown as dashed line (red or grayscale) superimposed over the black profiles. Note that the energy range of modeled SO_2 lines is 19–121 K.

4. Discussion

4.1. Dynamical Interpretation of the Line Profiles

From H_2O maser measurements, Richards et al. (1996) suggested the existence of a bipolar outflow in NML Cyg, oriented NW-SE at a position angle of 150°. This conclusion was based on a maser clump ~250 mas northwest of the star with LSR velocities ~5 km s^{-1}, and a less prominent group to the southeast with velocities near 20 km s^{-1}. However, strong blueshifted maser emission was also present near –22 km s^{-1}, close to the star. Subsequently, it was proposed that the masers were located on one side of the star, opposite the Cyg OB2 association (Schuster et al. 2009); a bipolar outflow centered on the star with a position angle of 108° was also suggested (Nagayama et al. 2008). More recently, Zhang et al. (2012a) concluded that the masers were asymmetrically distributed.

The line profiles in NML Cyg suggest the presence of two randomly oriented outflows, one blueshifted and the other redshifted with respect to the line of sight. The blue component points to the observer, but oriented $37° \pm 3°$ from the line of sight, with $V_{LSR} = -21 \pm 3$ km s^{-1}. The redshifted wind points away from the observer and is at an angle of $14° \pm 3°$ from the line of sight, with $V_{LSR} = 15 \pm 3$ km s^{-1} (Table 2). The modeling cannot distinguish whether the orientation is NW, SW, NE, or SE. Both outflows are clearly not oriented 180° with respect to each other, however, ruling out a bipolar geometry. The typical cone angle swept out by the blue and red outflows are $46° \pm 3°$ and $49° \pm 3°$, respectively. The red outflow is more extensive, reaching a radial distance of ~650 R_*, or 5″ from the star. The blue wind extends out to ~500 R_* (4″). The uncertainty in radial distribution is between 10% and 20%.

The spherical outflow encompasses a smaller area, with a maximum radius of ~3″ (330 R_*), as observed in CO (Table 1). Metal-bearing species (NaCl, AlO) are confined to the inner part of the shell with $r_{outer} < 50$ R_*; the other molecules typically extend out to 140–300 R_*. The central velocities of the spherical component are $V_{LSR} \sim -1$–3 ± 2 km s^{-1}, as proposed by others ($V_{LSR} = -1$–0 ± 2 km s^{-1}; Kemper et al. 2003; Etoka & Diamond 2004). A radial extent of 3″–5″ is consistent with the intensities of CO observed with the JCMT, which has a smaller beam size than the SMT (e.g., Kemper et al. 2003). The envelope around NML Cyg is therefore fairly extended with respect to the observed dust emission.

The exact orientation of the asymmetric flows cannot be determined from the fits. However, a sensitive HST image (F555W; 5337 Å) of NML Cyg shows an asymmetric, kidney-shaped nebula on scales of ~0.″25 (Schuster et al. 2006, 2009), extending NE–SE. The blueshifted and redshifted molecular outflows roughly follow the two lobes, projected onto the plane of the sky, if oriented to the NE and SE, respectively. Figure 3 illustrates the proposed orientations of the blue and red molecular flows, indicated in white and overlaid on the HST image, as well as the dust shell at 11 μm (Schuster et al. 2009). The approximate positions of the blue- and redshifted H_2O maser clumps are also shown. Note that Schuster et al. (2009) also found hot dust NW of the star. There is strong maser emission to the NW (Richards et al. 1996), but the V_{LSR} of these lines is 4.8 km s^{-1}, linking this region to the spherical flow.

The proposed outflow orientation is consistent with the positions and velocities of the H_2O masers, although they trace smaller spatial scales of ~0.″1–0.″2 (Richards et al. 1996; Nagayama et al. 2008). Correlation between the velocities of water and OH masers and the asymmetric molecular outflows has been found for VY CMa (Ziurys et al. 2007). As shown in the right panel of Figure 3, the blue- and redshifted emission features from the SO_2 line profile ($J_{Ka,Kc} = 11_{3,9} \rightarrow 11_{2,10}$) have almost identical velocities to the H_2O masers (Nagayama et al. 2008). Velocities near 0 ± 10 km s^{-1} are part of the spherical flow. Maser emission at $V_{LSR} = -21$ km s^{-1}—the nominal velocity of the blue molecular outflow—is close to the star in position–

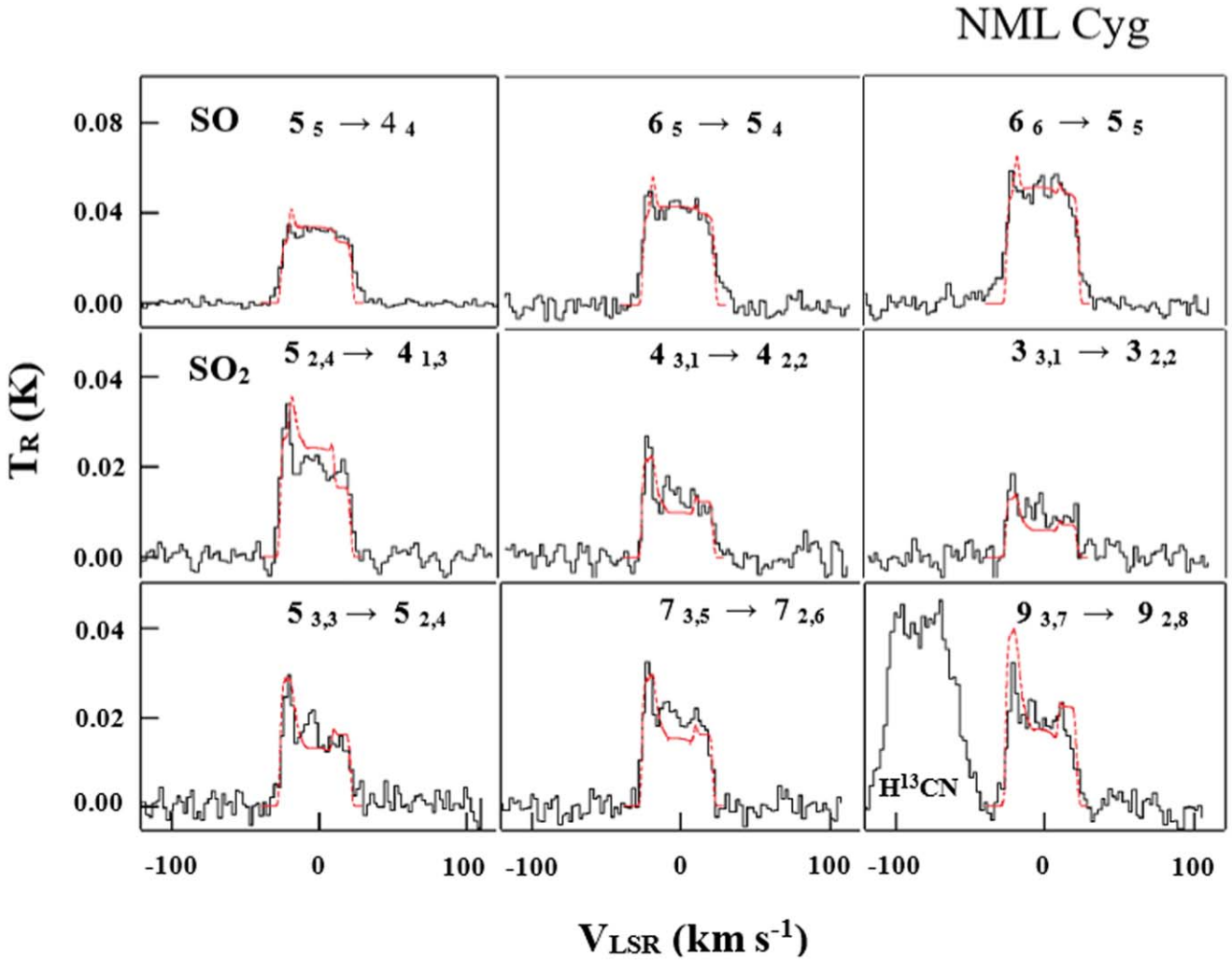

Figure 2. Sample spectra of SO_2 and SO observed toward NML Cyg (solid black; resolution: 2 MHz). Modeled line profiles are overlaid on the spectra (dashed red), based on a three-component fit (spherical flow, asymmetric red- and blueshifted winds).

Table 2
Multiple Component Fits to Select Molecules

Molecule	Outflow	Line of Sight Angle (°)	Cone Angle (°)	r_{peak} (R_*)	r_{outer} (R_*)	r_{outer} ($''$)	$n(H_2)_{peak}$	$f(X/H_2)$
SO_2	Blue	37	46	290	350	2.8	4.0×10^6	5.5×10^{-8}
	Red	14	49	310	460	3.7	3.5×10^6	1.2×10^{-8}
SO	Blue	37	46	310	350	2.8	4.0×10^6	3.0×10^{-8}
	Red	14	49	270	400	3.2	3.5×10^6	1.5×10^{-8}
CS	Blue	37	46	310	385	3.1	4.0×10^6	1.0×10^{-9}
	Red	14	49	330	385	3.1	3.5×10^6	1.0×10^{-9}
CO	Blue	31	39	365	500	4.0	7.5×10^5	9.0×10^{-5}
	Red	11	46	580	665	5.4	5.5×10^5	5.0×10^{-5}
HCO^+	Blue	37	49	365	480	3.9	1.5×10^5	2.5×10^{-8}
	Red	14	63	580	655	5.3	1.0×10^5	2.5×10^{-8}

velocity maps, but slightly shifted to the east (Richards et al. 1996). Similarly, the maser map at $V_{LSR} = 14.9$ km s^{-1}—the nominal velocity of the red wind—shows emission to the east/southeast of the star, but not to the southwest. Maser emission traces regions in the circumstellar envelope where the gas and dust accelerate to the envelope's terminal velocity (Richards et al. 1996). For NML Cyg, the red- and blueshifted masers likely indicate the base of the collimated molecular outflows, and their proper motion suggests the direction of these winds, which corresponds to distinct mass loss events. The upper limit to the outflow timescales is estimated at ∼1200–1300 yr, comparable to that of Arc 1 in VY CMa (Humphreys et al. 2007). Such events in supergiant stars such as Betelgeuse and VY CMa are thought to be generated by surface activity and "rogue" photospheric

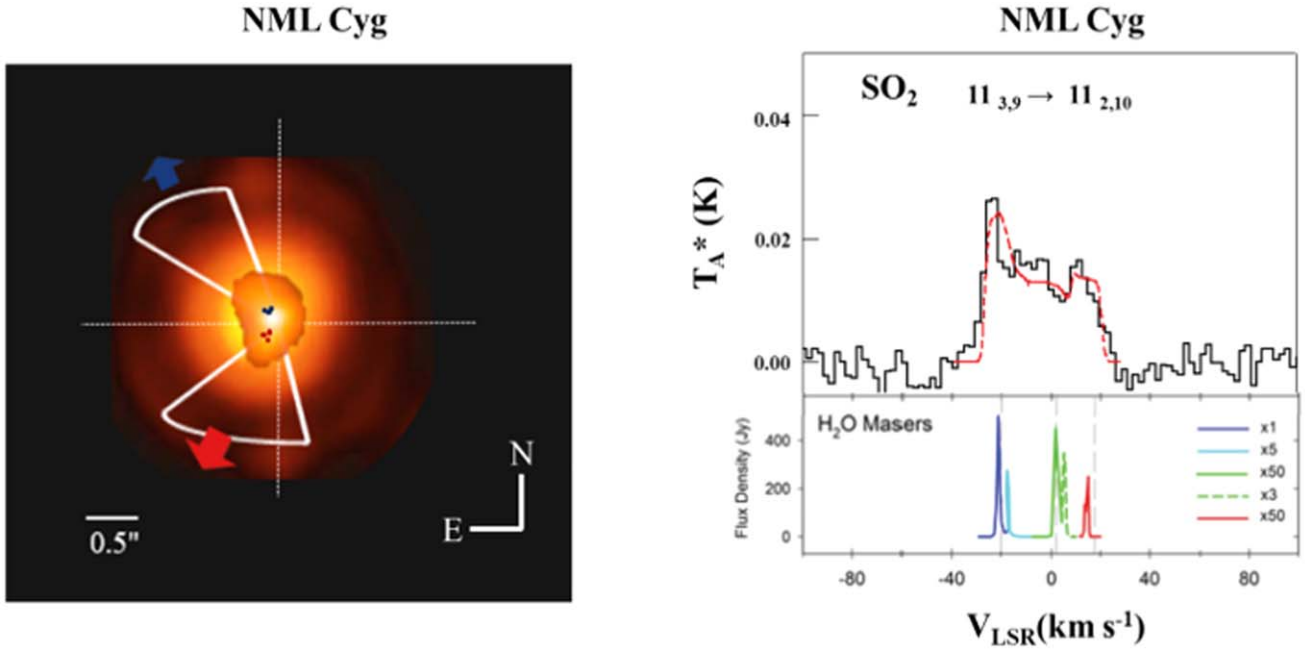

Figure 3. Left) Proposed geometry of the collimated molecular outflows in NM Cyg, projected onto the plane of the sky, superimposed over the 11 μm and HST images (Schuster et al. 2006, 2009). The blueshifted outflow (white, blue arrow) is oriented NE, ∼34° with respect to the line of sight; the redshifted wind (white, red arrow) is ∼12° from line of sight, shifted SE. Approximate positions of the red and blueshifted water masers are displayed. (Right) Spectrum of $J_{Ka,Kc} = 11_{3,9} \rightarrow 11_{2,10}$ line of SO_2 (upper panel) with three-component model fit superimposed in red. The water maser profile is shown (lower panel; Nagayama et al. 2008). The LSR velocities of the blue- and redshifted flows in SO_2 and the masers are well-aligned.

convection cells (Dupree et al. 2020; Montarges et al. 2021; Humphreys et al. 2021), although there are discrepancies in the relative timescales (see Chiavassa et al. 2009). NML Cyg appears to be yet another hypergiant star with this surface activity and may have undergone "dimming" as observed in VY CMa.

4.2. A Common Chemistry for Hypergiant Stars?

The number of chemical species found in NML Cyg is currently 21, including H_2; 17 are in the survey (Table 1). New molecular detections for this source include AlO, NaCl, PN PO, and NS (also see Rizzo et al. 2021). Of the 20 species identified, 10 contain oxygen, as perhaps expected. Carbon is also well-represented with CO, CN, CS, HCN, HNC, and HCO^+—the same C-bearing molecules found in VY CMa (Ziurys et al. 2009). Silicon is found in SiO and SiS, and sulfur through SiS, SO, SO_2, NS, and H_2S. Metal-bearing molecules observed are NaCl and AlO.

In terms of abundances for the spherical outflow, relative to H_2, CO has the highest with $f \sim 3.5 \times 10^{-4}$. The carbon is apparently contained primarily in CO, as expected (see Quintana-Lacaci et al. 2007), with the remaining sequestered with sulfur and nitrogen. CN and HCN carry nonnegligible amounts of carbon: $f \sim 2.0 \times 10^{-7}$ and 3.6×10^{-7}, respectively. The abundances of CS and HNC are about an order of magnitude lower. SiO and SiS are also prevalent, with $f \sim 8 \times 10^{-7}$ and 3.5×10^{-7}. Sulfur is principally contained in oxides ($f(SO) \sim 3.5 \times 10^{-7}$, $f(SO_2) \sim 6.5 \times 10^{-7}$) and hydrides ($f(H_2S) \sim 4.5 \times 10^{-6}$). NS is a minor carrier with $f \sim 10^{-9}$. Of the more refractory species, PO is the highest abundance ($\sim 10^{-8}$), followed by AlO, NaCl, and PN (~ 3–6×10^{-9}). In terms of radial distributions, CO and HCN are clearly the most extended at $r_{outer} > 300\ R_*$; the most confined species are NaCl and AlO ($r_{outer} < 45\ R_*$). The phosphorus-bearing species do not condense out as rapidly and remain in the gas into the outer envelope.

The asymmetric outflows are best traced in SO_2 and SO, as for VY CMa. HCO^+ is blended with SO_2 in this survey, but other uncontaminated transitions appear to be present only in the asymmetric flows (Pulliam et al. 2011). The appearance of certain species in these ejecta may be a result of selective chemistry. HCO^+ may be formed from CO in ion-molecule reactions, while SO and SO_2 may require shock processing (Adande et al. 2013). In the asymmetric winds, molecular abundances typically drop by about a factor of 10–15, relative to the spherical flow, and they extend further out. Red supergiant/hypergiant stars are thought to undergo episodic, local ejection of gas clumps from the photosphere (Dupree et al. 2020; Montarges et al. 2021; Humphreys et al. 2021). Such ejecta are the origin of the blue- and redshifted flows in NML Cyg, which may also contain material swept up from the spherical wind.

The envelopes of NML Cyg and VY CMa contain similar abundances. In the spherical wind of VY CMa, SO and SO_2 have $f \sim 3 \times 10^{-7}$—almost identical to those in NML Cyg—and the NaCl, PN and PO abundances are within a factor of 2 (Milam et al. 2007; Ziurys et al. 2018). There appears to be some variation in the carbon chemistry, with CO having a slightly lower abundance in VY CMa ($f \sim 4 \times 10^{-5}$), but higher in HCN ($f \sim 10^{-6}$). The values are in part model-dependent, relying on the accuracy of databases, spectral sensitivity, and the number of observed transitions. Further studies are necessary for a more detailed assessment.

This work was supported by NSF grant AST-1907910.

ORCID iDs

A. P. Singh https://orcid.org/0000-0002-5419-183X
R. M. Humphreys https://orcid.org/0000-0003-1720-9807
L. M. Ziurys https://orcid.org/0000-0002-1805-3886

References

Adande, G. R., Edwards, J. L., & Ziurys, L. M. 2013, ApJ, 778, 22
Boboltz, D. A., & Claussen, M. J. 2004, ApJ, 608, 480
Chiavassa, A., Plez, B., Josselin, E., & Freytag, B. 2009, A&A, 506, 1351
Davies, B., & Beasor, E. R. 2020, MNRAS, 493, 468
De Beck, E., Vlemmings, W., Muller, S., et al. 2015, A&A, 580, A36
Decin, L., Richards, A. M. S., Millar, T. J., et al. 2016, A&A, 592, A76
Dubernet, M. L., Boudon, V., Culhane, J. L., et al. 2010, JQSRT, 111, 2151
Dupree, A., Strassmeier, K. G., Matthews, L. D., et al. 2020, ApJ, 899, 68
Etoka, S., & Diamond, P. 2004, MNRAS, 348, 34
Gordon, M. S., Humphreys, R. M., & Jones, T. J. 2016, ApJ, 825, 50
Humphreys, R. M., Davidson, K., Richards, A. M. S., Ziurys, L. M., Jones, T. J., & Ishibashi, K. 2021, AJ, 161, 98
Humphreys, R. M., Helton, L. A., & Jones, T. J. 2007, AJ, 133, 2716
Humphreys, R. M., Ziurys, L. M., Bernal, J. J., et al. 2019, ApJL, 874, L26
Justtanont, K., Jong, T. de, Helmich, F. D., et al. 1996, A&A, 315, L217
Kaminski, T. 2019, A&A, 627, A114
Kamiński, T., Gottlieb, C. A., Menten, K. M., et al. 2013, A&A, 551, A113
Kemper, F., Stark, R., Justtanont, K., et al. 2003, A&A, 407, 609
Milam, S. N., Apponi, A. J., Woolf, N. J., et al. 2007, ApJL, 668, L131
Monnier, J. D., Bester, M., Danchi, W. C., et al. 1997, ApJ, 481, 420
Montarges, M., Cannon, E., Lagadec, E., et al. 2021, Natur, 594, 365
Müller, H. S. P., Schlöder, F., Stutzki, J., & Winnewisser, G. 2005, JMoSt, 742, 215
Nagayama, T., Koji, T., Toshihiro, O., et al. 2008, PASJ, 60, 1069
O'Gorman, E., Vlemmings, W., Richards, A. M. S., et al. 2015, A&A, 573, L1
Pickett, H. M., Poynter, R. L., Cohen, E. A., et al. 1998, JQSRT, 60, 883
Pulliam, R. L., Edwards, J. L., & Ziurys, L. M. 2011, ApJ, 743, 36
Quintana-Lacaci, G., Bujarrabal, V., Castro-Carrizo, A., & Alcolea, J. 2007, A&A, 471, 551
Richards, A. M. S., Yates, J. A., & Cohen, R. J. 1996, MNRAS, 282, 665f
Rizzo, J. R., Cernicharo, J., & Garcia-Miro, C. 2021, ApJS, 253, 44
Schuster, M. T., Humphreys, R. M., & Marengo, M. 2006, AJ, 131, 603
Schuster, M. T., Marengo, M., Hora, J. L., et al. 2009, ApJ, 699, 1423
Shenoy, D., Humphreys, R. M., Jones, T. J., et al. 2016, AJ, 151, 51
Smartt, S. 2009, ARA&A, 47, 63
Smartt, S. 2015, PASA, 32, E016
Tenenbaum, E. D., Dodd, J. L., Milam, S. N., Woolf, N. J., & Ziurys, L. M. 2010a, ApJL, 720, L102
Tenenbaum, E. D., Dodd, J. L., Milam, S. N., Woolf, N. J., & Ziurys, L. M. 2010b, ApJS, 190, 348
Tenenbaum, E. D., & Ziurys, L. M. 2010, ApJL, 712, L93
Tennyson, J., & Yurchenko, S. N. 2012, MNRAS, 425, 21
Teyssier, D., Quintana-Lacaci, G., Marston, A. P., et al. 2012, A&A, 545, A99
Tiffany, C., Humphreys, R. M., Jones, T. J., & Davidson, K. 2010, AJ, 140, 339
van Loon, J. T., Cioni, M.-R. L., Zijlstra, A. A., & Loup, C. 2005, A&A, 438, 273
Ysard, N., Jones, A. P., Demyk, K., Boutéraon, T., & Koehler, M. 2018, A&A, 617, A124
Zhang, B., Reid, M. J., Menten, K. M., & Zheng, X. W. 2012b, ApJ, 744, 23
Zhang, B., Reid, M. J., Menten, K. M., Zheng, X. W., & Brunthaler, A. 2012a, A&A, 544, A42
Ziurys, L. M., Milam, S. N., Apponi, A. J., & Woolf, N. J. 2007, Natur, 447, 1094
Ziurys, L. M., Schmidt, D. R., & Bernal, J. J. 2018, ApJ, 856, 16
Ziurys, L. M., Tenenbaum, E. D., Pulliam, R. L., Woolf, N. J., & Milam, S. N. 2009, ApJ, 695, 1604
Zubko, V., Li, D., Lim, T., Feuchtgruber, H., & Harwit, M. 2004, ApJ, 610, 427